Propagation of structured light through tissue-mimicking phantoms

ALESSIA SUPRANO,[1] TAIRA GIORDANI,[1] ILARIA GIANANI,[1]
NICOLÓ SPAGNOLO,[1] KATJA PINKER,[2] JUDY KUPFERMAN,[3]
SHLOMI ARNON,[3] UWE KLEMM,[4,5] DIMITRIS GORPAS,[4,5] VASILIS
NTZIACHRISTOS,[4,5] AND FABIO SCIARRINO[1,6,*]

[1]*Dipartimento di Fisica, Sapienza Università di Roma, P.le Aldo Moro, 5, 00185 Rome, Italy*
[2]*Department of Biomedical Imaging and Image-guided Therapy, Molecular and Gender Imaging Service, Medical University of Vienna, Waehringer Guertel 18-20, 1090 Vienna, Austria*
[3]*Electrical and Computer Engineering Department, Ben-Gurion University of the Negev, P.O. Box 653 IL-8441405, Beer Sheva, Israel*
[4]*Institute of Biological and Medical Imaging, Helmholtz Zentrum München, Ingolstädter Landstrasse 1, Neuherberg D-85764, Germany*
[5]*Chair of Biological Imaging and TranslaTUM, Technical University of Munich, Ismaningerstr. 22, D-81675 Munich, Germany*
[6]*Consiglio Nazionale delle Ricerche, Istituto dei sistemi Complessi (CNR-ISC), Via dei Taurini 19, 00185 Roma, Italy*
[*]fabio.sciarrino@uniroma1.it

Abstract: Optical interrogation of tissues is broadly considered in biomedical applications. Nevertheless, light scattering by tissue limits the resolution and accuracy achieved when investigating sub-surface tissue features. Light carrying optical angular momentum or complex polarization profiles, offers different propagation characteristics through scattering media compared to light with unstructured beam profiles. Here we discuss the behaviour of structured light scattered by tissue-mimicking phantoms. We study the spatial and the polarization profile of the scattered modes as a function of a range of optical parameters of the phantoms, with varying scattering and absorption coefficients and of different lengths. These results show the non-trivial trade-off between the advantages of structured light profiles and mode broadening, stimulating further investigations in this direction.

1. Introduction

The study of light-tissue interaction has attracted considerable interest in the past decades for better understanding possibilities to develop sensors and imaging methods for disease diagnostics and management. Of particular importance has been the development of methods that can measure tissue parameters deeper than the penetration limits of optical microscopy [1]. Optical imaging uses non-ionizing radiation and can be made portable and cost-effective, offering a valuable tool for biomedical interrogations. Several optical technologies have now been considered or approved for clinical applications, including optical coherence tomography (OCT) [2], autofluorescence imaging (AFI) [3], or fluorescence molecular imaging (FMI) [4] have already gained approvals for clinical use. For example, OCT finds great clinical acceptance for ophtalmologic fundus [5,6] and intravascular imaging [7], AFI for endoscopic [8] and ophtalmologic fundus imaging [9], and FMI for surgical guidance [10,11]. However, one limiting factor of optical imaging is the strong dependence of the signals collected on the tissue optical properties [12]. Propagation of light through a dense medium with optical properties similar to those of tissue is governed by the influence of wavelength dependent scattering and absorption, resulting in limited penetration depth and low resolution readouts due to photon diffusion. The adoption of structured light might

help mitigate these effects [13–20]. Indeed, light carrying orbital angular momentum (OAM) as well as light obtained as a superposition of different OAM modes, namely vector vortex beams (VVB) [13,21–24], appear to be viable candidates for improving transmission through scattering media [16,25–30]. In this regard, structured light finds many applications in several endeavors where robustness to propagation is required [31–44].

Among this,VVBs can be a useful resources for optical wireless communication (OWC), both classical and quantum [45–49]. Use of polarization states as well as OAM in optical communication has been extensively developed [50], with particular application in secure communications and quantum key distribution (QKD). This has been extended to VVBs, even at the single photon level [42,51] and quantum key distribution too has been demonstrated using VVBs [41,52]. In particular, information can be encoded in different combinations of polarization and OAM. Two polarization bases are used: horizontal/vertical (H/V) and diagonal/antidiagonal (D/A). These are combined with two different OAM modes, sufficiently distant to afford easy distinction between them. However, communication protocols can be affected by the VVBs interaction with scattering and turbulent media [38,39]. Therefore, a deep comprehension of the consequences of this interaction on the VVBs features is of crucial interest.

In this paper we evaluate the behavior of structured light interacting with tissue-mimicking phantoms, by observing the spatial characteristics and polarization profile of the scattered beams. The phantoms employed in the analysis vary in length, scattering and absorption properties, providing a comprehensive insight on the dependence of light to optical properties and thickness. In the following we discuss the phantoms employed, experimental setup and the structured states of light employed for phantom interrogation.

2. Phantoms

Table 1. Phantom compositions. The density of TiO_2 grows along rows, while the density of Nigrosine increases along columns. The optical density (OD) parameters are computed for the samples with length of 0.5 mm and an incident beam with $m = 5$ ($OD = \log_{10}(\frac{I_0}{I_T})$). I_0 is the intensity of the incident beam, which is obtained by summing up the intensities of each pixel of the collected image, and I_T is the transmitted intensity, which is estimated with a similar procedure. Since these datasets were not measured to study the sample behaviour as a function of OD coefficients, possible other effects may not be observed in our measurement conditions.

Set 1	Set 2	Set 3	Set 4
TiO_2 : 0.75 mg/g	TiO_2 : 1.5 mg/g	TiO_2 : 3 mg/g	TiO_2 : 6 mg/g
Nigrosine: 0.004375 mg/g	Nigrosine: 0.004375 mg/g	Nigrosine: 0.004375 mg/g	Nigrosine: 0.004375 mg/g
OD: 1.49	OD: 1.57	OD: 2.92	OD: 3.12
Set 5	**Set 6**	**Set 7**	**Set 8**
TiO_2 : 0.75 mg/g	TiO_2 : 1.5 mg/g	TiO_2 : 3 mg/g	TiO_2 : 6 mg/g
Nigrosine: 0.00875 mg/g	Nigrosine: 0.00875 mg/g	Nigrosine: 0.00875 mg/g	Nigrosine: 0.00875 mg/g
OD: 1.24	OD: 1.57	OD: 2.92	OD: 3.13
Set 9	**Set 10**	**Set 11**	**Set 12**
TiO_2 : 0.75 mg/g	TiO_2 : 1.5 mg/g	TiO_2 : 3 mg/g	TiO_2 : 6 mg/g
Nigrosine: 0.0175 mg/g	Nigrosine: 0.0175 mg/g	Nigrosine: 0.0175 mg/g	Nigrosine: 0.0175 mg/g
OD: 1.29	OD: 1.50	OD: 2.93	OD: 3.12
Set 13	**Set 14**	**Set 15**	**Set 16**
TiO_2 : 0.75 mg/g	TiO_2 : 1.5 mg/g	TiO_2 : 3 mg/g	TiO_2 : 6 mg/g
Nigrosine: 0.035 mg/g	Nigrosine: 0.035 mg/g	Nigrosine: 0.035 mg/g	Nigrosine: 0.035 mg/g
OD: 1.26	OD: 1.50	OD: 2.92	OD: 3.11

The study presented herein was implemented using phantoms of different optical properties, i.e. absorption (μ_a) and scattering (μ_s) coefficients, and length. The phantoms were developed adopting the recipe employed in a previous study proposing of our group for fluorescence imaging standardization [53,54]. In specifics, the main constituent of the phantoms was transparent polyurethane (WC-783 A/B, BJB Enterprises, Tustin, United States), while scattering was imposed by use of anatase TiO_2 nanoparticles (Titanium IV Oxide, Sigma Aldrich, St. Louis, United States) and absorption by alcohol soluble nigrosin (Sigma Aldrich). The selection of the specific materials was based on the stability of their optical properties over time and their ability to create homogeneous mixtures [55,56]. In Table 1 we report the properties by means of concentration of 16 phantom sets. As can be seen in this table, the ratio between scattering and absorption remains constant along the diagonal. Each phantom set with the same optical properties consists of 8 phantoms with length spanning from 0.5 mm to 7.0 mm.

3. Experiments

Interactions with scattering and absorbing media with optical properties mimicking those of human tissue have several effects on the propagated light. The scattering component heavily affects the spatial resolution, the transmitted intensity is attenuated as a function of distance, absorption and scatter, and the polarization of the transmitted light undergo modifications.

The phantoms were interacted with structured states of light [21,22]. Beams carrying angular momentum, such as the spin (SAM) and orbital angular momentum (OAM) [24], display distinctive properties for what concerns the spatial relationships among the points of the wave-front as well as the polarization distribution [23,57]. OAM states of light are scalar field carrying a phase term $e^{im\phi}$, where ϕ is the azimuthal phase and m an integer number. The resulting beam is an optical vortex with a singularity on the propagation axis: the number m represents the topological charge, i.e the winding number around the singularity [21]. When this phase is coupled with the vectorial properties of the beam, such as the polarization, one can obtain a non-uniform distribution of the polarization on the wave-front, i.e a vector field. We then introduce *vector vortex beams* (VVBs) as general states with non-trivial SAM and OAM, which result from the superposition of two fields with different charges, m_1 and m_2, and orthogonal circular polarization $\{R, L\}$ [23]. Although we treat fields as classical, we use Dirac notation for clarity, as follows:

$$|VVB\rangle = \cos\frac{\theta}{2}|R, m_1\rangle + e^{i\phi}\sin\frac{\theta}{2}|L, m_2\rangle, \tag{1}$$

where $\theta \in [0, \pi]$ and $\phi \in [0, 2\pi]$ are real parameters. Each state in the form of 1 displays peculiar properties with respect to the spatial and polarization intensity distribution. Indeed the points in transverse plane are strongly correlated in these two degrees of freedom. Hence, the VVBs are very interesting probes for investigating how scattering and absorption properties of human tissues modify the coherence relationships that identify structured light [14,16].

The experimental setup for generating structured light is displayed in Fig. 1. The initial beam, prepared with zero OAM and a fixed polarization, is converted to the desired angular momentum state by a system of 5 q-plates [58,59]. The q-plates are inhomogenous birefringent waveplates whose optical axis orientation presents a singularity in the centre of the plate's plane, with a topological charge equal to q. In this way the beam after propagating through a q-plate acquires a phase term $e^{\pm 2iq\phi}$ according to the polarization state [60], resulting in an increment of the OAM equal to $\Delta m = 2q$. In particular the q-plate operation is equivalent to the conversion of SAM into OAM. Indeed we have:

$$\begin{aligned}
|L, m\rangle &\xrightarrow{q-plate} |R, m + 2q\rangle \\
|R, m\rangle &\xrightarrow{q-plate} |L, m - 2q\rangle
\end{aligned} \tag{2}$$

The combined actions of q-plates, along with half- and quarter-waveplates in between, allow to modulate the spatial and polarization properties to generate states as in 1. Then the beam propagates in the sample and the scattered light is collected by an objective. Observation of exiting spatial beam profile is performed by placing a camera in the pupil plane of the objective. In order to perform the polarization analysis we collimate the beam, so as to insert the polarization measurement components and then we use a second lens to image the beam onto the camera.
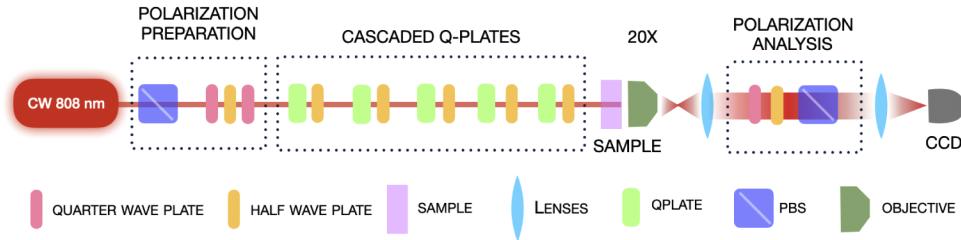

Fig. 1. Experimental Setup. A continous wave laser (CW) source (CNI Laser PSU-III-FDA) at 808 nm, is shaped into the desired OAM or VVB mode by a squence of 5 q-plates, alternated with half and quarter wave plates. After the interaction with the sample, the transmitted light is collected by means of a 20x objective. The beam is then collimated using a lens with focal length f = 30 mm and imaged on a CCD camera (Thorlabs DCU223C) with a lens of focal length f = 50 mm. For the polarization analysis, a quarter wave plate, an half wave plate and a polarizing beam spitter (PBS) are added after the beam collimation to record the Stokes parameters.

Experimental measurements were obtained from all phantom sets listed in Table 1, after illumination by OAM modes with $m = \{1, 3, 5\}$ and VVB modes with $(m_1, m_2) = \{(-1, 1), (-3, 3), (-5, 5), (-3, 1), (-5, 3)\}$.

4. Results

4.1. Measurements of the beam profiles

Analysis of the beam profiles collected after propagation in the diffusive phantoms is performed by observing the two intensity peaks revealed in profiles selected along the x axis (Fig. 2). Figure 2 shows an example of the recorded beam profile and the corresponding intensity distribution along the x direction in the transverse plane obtained for the referenced LG mode with $m = 5$, measured without the sample, and for the same state after the propagation through samples characterized by lengths equal to $L = 4, 7$ mm, TiO_2 and Nigrosine concentration of 0.75 mg/g and 0.000875 mg/g, respectively.

Figure 2 shows clearly how the intensity peaks are broadened as a result of the scattering from the media. Moreover, in contrast to the first spatial mode whose profile is described by two gaussian peaks, after the propagation in the scattering media the peaks can be fitted using Lorentzians with increasing *FWHM* (full width at half maximum) as a function of the sample length. This degradation of the spatial resolution is at variance with other scattering media such as latex beads where it is due exclusively to an additional background noise [30].

In addition to the broadening quantification, obtained computing the parameter $FWHM_{s,l}/FWHM_0$, we quantify the spatial resolution according to the Rayleigh criteria. We thus calculate the following quantity:

$$R_{s,l} = \frac{c_1 - c_2}{FWHM_{s,l}}, \tag{3}$$

where c_i are the peak's center coordinates and $FWHM_{s,l}$ is the full width half-maximum after the propagation in the sample s of length l.
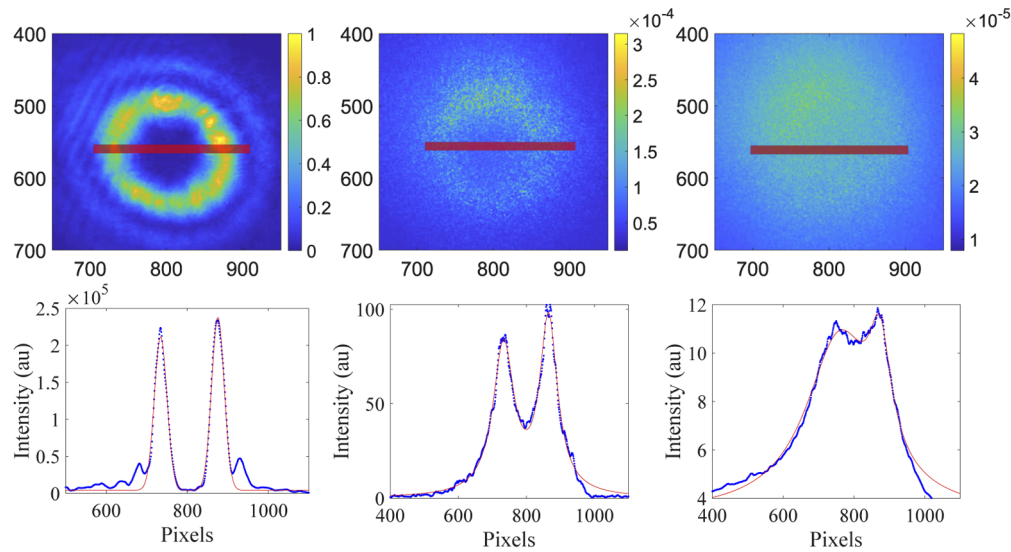
Fig. 2. Spatial contrast. a) Spatial modes associated to the referenced state $m = 5$, measured without the sample, and to the same state after the propagation through samples with length 4 mm and 7 mm, respectively, at fixed scattering and absorption values (TiO_2 : 0.75 mg/g Nigrosine: 0.00875 mg/g) b) Fit of the spatial profile selected through a slice, for the same modes of the above panel. The transmitted intensity undergoes a substantial decrease and, in contrast to the referenced mode, which is fitted with a Gaussian function, the other two modes are fitted with a Lorentzian function.

In Fig. 3, we report the results associated to the broadening parameter and to the Rayleigh parameter, for all the spatial modes examined. The graphs show the behaviours as a function of the scattering and absorbing properties and of the phantoms length, as two of these three parameters are kept fixed for each graph. We note that while there is a clear trend when increasing the TiO_2 concentration and sample length, the effect of Nigrosine is negligible.

In particular, as shown in Fig. 3(b,e) the broadening of the *FWHM* of the spatial peaks due to the interaction with the scattering media is greater for OAM modes with larger m. This implies a faster decreasing of the Rayleigh parameter for such modes. Nevertheless, these states are characterized by a larger shape of the mode, which results in further separated spatial peaks (as reflected by a large $(c_1 - c_2)$). This feature motivates the observation, in the analyzed range of phantom properties, of a higher Rayleigh parameter than that reached by OAM modes with lower m despite the fact that the spatial peaks for higher m are more broadened by the interaction (Fig. 3(a-d)). Similarly to the OAM modes, the VVB behaviour depends on the m values that characterize them, and in particular on the internal and external radius of the donuts. The spatial agreement between the VVB modes $(m_1, m_2) = \{(-1, 1), (-3, 3), (-5, 5)\}$ and the LG modes with $m = \{1, 3, 5\}$, respectively, motivates the similarity of behaviors. However, for modes with $|m_1| \neq |m_2|$ there is an interplay between the m_i of the two superimposed modes. For example, mode $(-3, 1)$ is characterized by the internal radius equal to the state $m = 1$ but with a higher broadening compared to its respective OAM mode $m = 1$ due to the superposition with $m = -3$, which will affect the values of R. This is even more evident for mode $(-5, 3)$, where the broadening due to $m = -5$ compared to the state $m = 3$, influences its intermediate behaviour. In conclusion, for both OAM and VVB modes, the resolution trend depends on the broadening of the spatial features. However, since the peaks are separated by different lengths depending on the mode profile, there is an interplay between this separation and the broadening of the *FWHM* due to the interaction with the media.
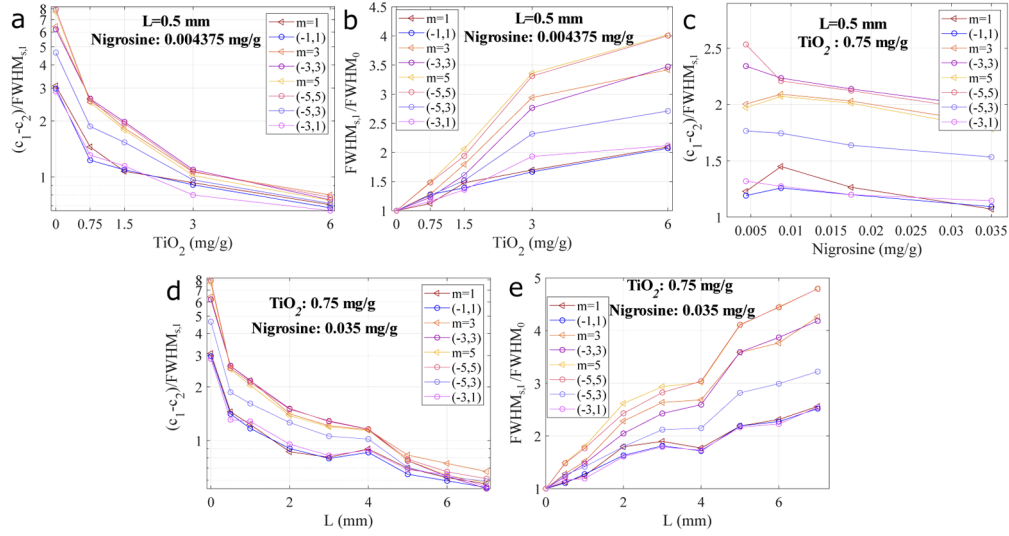
Fig. 3. Spatial contrast analysis for different samples and modes. a) Semi-logarithmic scale to represent the Rayleigh parameter as a function of TiO_2 for LG modes with $m = \{1, 3, 5\}$ and VVB modes with $(m_1, m_2) = \{(-1, 1),(-3, 3),(-5, 5),(-3, 1),(-5, 3)\}$. The sample length and the Nigrosine concentration are kept fixed: $L = 0.5$ mm and the $\mathcal{N} = 0.004375$ mg/g. b) Ratio between *FWHM* with sample and without sample for all the modes of the previous panel and for the same fixed length and Nigrosine concentration. The ratio is always greater than 1, confirming the broadening, much more evident for larger m. c) Rayleigh parameter as a function of Nigrosine concentration ($\mathcal{N}$) at a fixed values of the sample length $L = 0.5$ mm and of the TiO_2 concentration 0.75 mg/g. The Rayleigh parameter seems to be almost insensitive to $\mathcal{N}$. d) Semi-logarithmic scale to represent the Rayleigh parameter as a function of sample length for all the previously considered OAM and VVB modes at fixed Nigrosine (0.035 mg/g) and TiO_2 (0.75 mg/g) concentrations. The retrieved behaviour is similar to that found for the analysis in a) with respect TiO_2 concentration. e) Ratio between *FWHM* with sample and without sample for all the modes of the previous panel and for the same fixed TiO_2 and Nigrosine concentration. As in analysis performed in the panel b) with respect TiO_2 concentration, the ratio confirms a broadening, much more evident for larger m.

4.2. Polarization measurements

We have performed the polarization analysis by estimating the depolarization ratio (*DR*) for the VVBs and for the Laguerre Gauss modes (OAM) for all the samples reported in Table 1. The measurements have been carried out with the same setup reported in Fig. 1 by inserting the polarization analysis components (dotted square) before recording the image with the CCD. In this way, we were able to acquire the polarization distribution for all the vector vortex beams as well as for the LG modes, resolved in the coordinates (x, y) in the polarization basis $b = \{(H, V), (D, A), (L, R)\}$. From these images we have reconstructed the Stokes parameters

$$S_1 = \frac{I_H - I_V}{I_H + I_V}; \quad S_2 = \frac{I_D - I_A}{I_D + I_A}; \quad S_3 = \frac{I_R - I_L}{I_R + I_L}, \quad (4)$$

where I_b corresponds to the intensity in the polarization basis b.

The polarization pattern can be visualized in a single image by using a RGB map associated to the three Stokes parameters. In the panel a) of Fig. 4, the polarization profiles recorded for the VVBs characterized by $(m_1, m_2) = \{(-1, 1),(-3, 3),(-5, 5),(-3, 1),(-5, 3)\}$ are reported for different lengths $L = 0.5, 2, 4$ mm at a fixed concentration of Nigrosine (0.004375 mg/g) and

TiO$_2$ (0.75 mg/g). These maps show clearly how the information stored in the spatial structure of the polarization distribution can be lost as a result of the propagation in the scattering media. Furthermore, VVBs that display a more complex polarization pattern are more affected by the scattering process. To study in details this first observation, we define the depolarization ratio
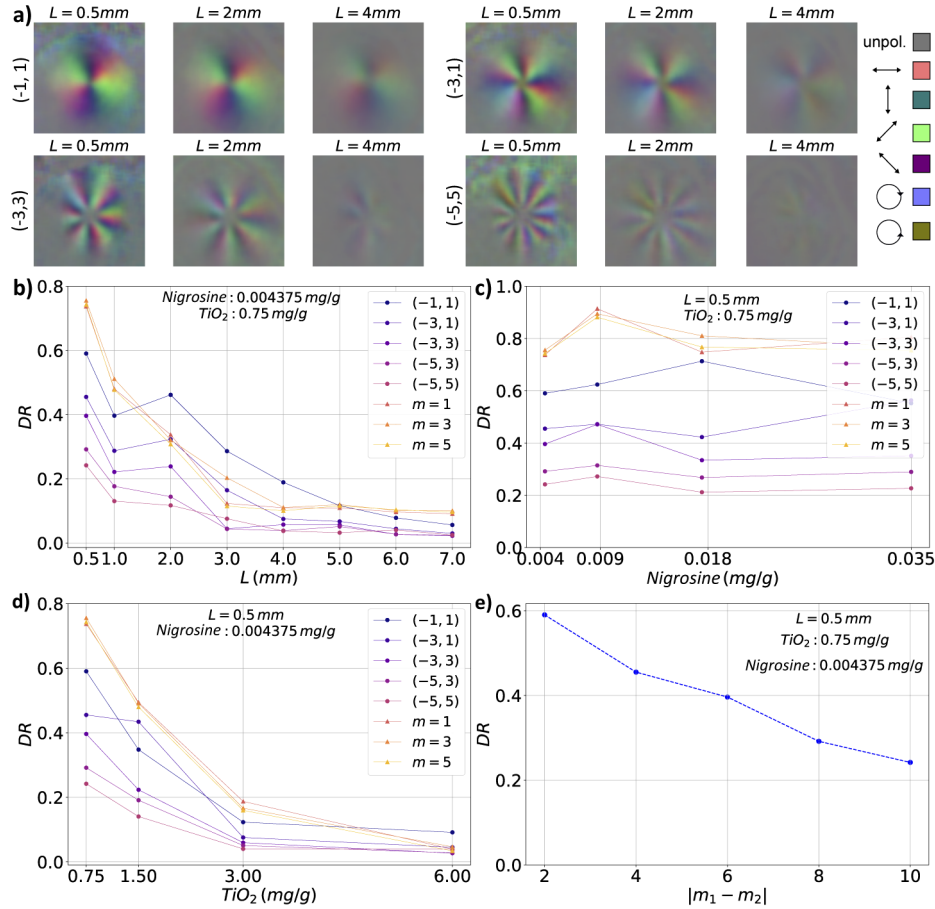

Fig. 4. Polarization analysis a) Polarization patterns encoded in the colors listed in the inset, for several VVBs with $(m_1, m_2) = \{(-1, 1), (-3, 3), (-5, 5), (-3, 1), (-5, 3)\}$ and samples lengths $L = \{0.5\,mm, 2\,mm, 4\,mm\}$, and fixed concentration of TiO$_2$: $0.75\,mg/g$ and Nigrosine, $\mathcal{N} = 0.004375\,mg/g$. The beams tend to be unpolarized for increasing lengths and more quickly for higher values of the quantity $|m_1 - m_2|$. b) Complete analysis of the scalar OAM modes and set of VVBs (see the legend in the plot) of the depolarization ratio (*DR*) for different sample lengths at fixed TiO$_2$ and $\mathcal{N}$. OAM eigenstates behave in the same way independently by the m value, while the VVBs display different trends according to (m_1, m_2). c) Analysis with respect $\mathcal{N}$ concentration, i.e the absorption, at fixed sample length and TiO$_2$ concentration. The *DR* of all the beams does not display any significant dependence from Nigrosine concentration. d) Trends for different value of scattering centre concentration, i.e TiO$_2$ concentration, at fixed length and $\mathcal{N}$. We retrieve similar behaviours found for the analysis in b) with respect samples lengths. e) Focus on the *DR* only for VVB at fixed lengths, scattering and absorption as a function of $|m_1 - m_2|$. Scattering affects the VVB with more complex spatial distribution of the polarization pattern, resulting in a smaller *DR*.

(*DR*), which quantifies the polarization regardless of its orientation (H, V, A, D, L, R), as:

$$DR = \sqrt{(S_1)^2 + (S_2)^2 + (S_3)^2}. \tag{5}$$

Our measurement stage allows to evaluate Stokes parameters at each camera's pixel. Then the *DR* has been averaged over pixels corresponding to the beam area. In particular we consider the area of the doughnut identified by the inner radius equal to $\rho - FWMH$ and the outer $\rho + FWMH$, where ρ is the radius of maximum intensities, given by the previous analysis on the spatial properties. Then, in Fig. 4 we report the *DR* parameter for all VVB and OAM modes as a function of sample length (b), absorption (c) and scattering (d). We note that there is a clear *DR* decrease with respect to TiO$_2$ concentration and to the sample length, while the effect of Nigrosine is negligible. In particular, the *DR* value is higher for the OAM modes and it does not seem to depend from the m values. On the contrary, for VVBs that display a nonuniform polarization distribution, there is an evident trend as a function of the difference between the topological charges of the two modes superimposed in 1. This parameter reflects the complexity of the polarization structure as can be observed by the maps displayed in Fig. 4(a), in which the difference starts from 2 up to 10. In Fig. 4(e), we show the *DR* value for increasing differences between topological charges only for VVBs, at fixed sample length and scattering and the absorption centres concentrations. The *DR* displays an evident decrease with increasing values of the difference between these topological charges.

5. Discussion

In this paper we have experimentally investigated the propagation of structured light beams through tissue-mimicking phantoms of different optical parameters, i.e. varying scattering and absorption coefficients. The optical properties are varied in the different samples, by changing the concentration of scattering and absorption in the phantom composition. More specifically, we have studied changes in the exiting beam profiles the degradation in the spatial resolution and in the polarization pattern of OAM and vector vortex beams, after propagation through phantoms of different lengths.

The first analysis on the spatial effects on the beam profile has shown that broadening of the spatial profile increases for larger OAM values, while keeping fixed the optical properties of the scattering medium. In parallel, we observe for vector vortex beams that the *DR* has a faster decrease for larger values of the difference $|m_1 - m_2|$ between the two OAM components of the superposition state. Finally, we find that both physical effects (spatial profile and depolarization) depend on the propagation length and on the TiO$_2$ concentration, while being almost independent from the Nigrosine concentration imparting the absorption property. Moreover, the spatial and polarization profile is preserved although the decrease in the transmitted signal is considerable.

In Fig. 5, we summarize our findings for the specific case of the VVB mode with $(m_1, m_2) = (5, -5)$, which is characterized by the largest radius of the doughnut spatial distribution (quantified by $(c_1 - c_2)$) and a highly-complex polarization profile. Since our analysis shows that there is low dependence on the concentration of Nigrosine in the phantoms, we report the two characteristic behaviours for the Rayleigh parameter $R_{s,l}$ in Fig. 5(a) and of the depolarization rate *DR* in Fig. 5(b), as a function of the phantoms length l and TiO$_2$ concentration s. We note that for some values of these two parameters, the spatial resolution as well as the polarization pattern are completely lost; the mode loses its characteristic "doughnut" shape, making it impossible to evaluate the parameter R, and it also becomes completely unpolarized. These conditions appear for the same values of l and s, and are shown with an 'x' on the two maps.

Regarding degradation of the spatial resolution of the beam profile, we find a different behaviour with respect to previous studies [30] that analyzed the propagation of structured light through a different class of scattering media. Indeed, in [30] it was shown that, in the investigated concentration regime, scattered light through latex beads in water solution preserves its Gaussian
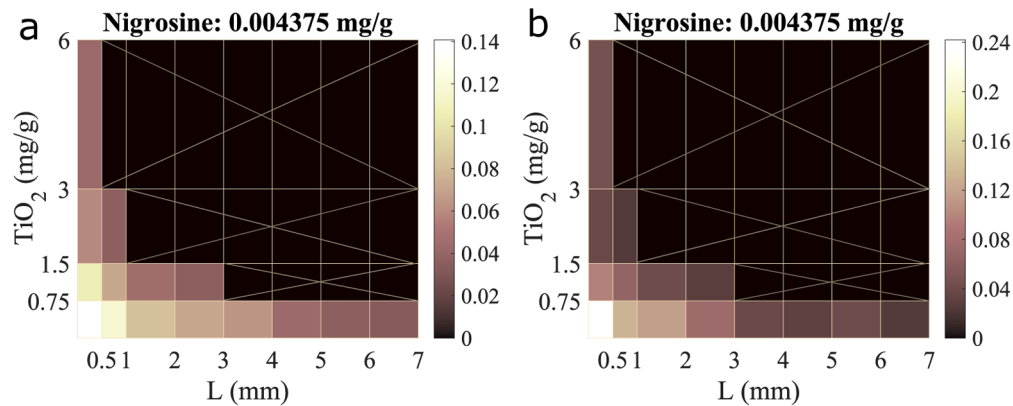
Fig. 5. Spatial and polarization behaviours. a) Rayleigh parameter $R_{s,l}$ of the mode $(-5, 5)$ as a function of scattering and sample length for fixed absorption. The regions marked with 'x' indicate the values of TiO_2 concentration and sampling length for which the spatial resolution is completely lost. b) Depolarization ratio DR of the mode $(-5, 5)$ as a function of scattering and sample length for fixed absorption. The regions marked with 'x' indicate the values of TiO_2 concentration and sampling length for which the mode appears completely unpolarized.

profile and contributes to the loss of resolution via additional background noise. Conversely, we find that, in the measured tissue-mimicking phantoms, the loss of resolution appears as a Lorentzian broadening of the spatial profile. These results show that latex beads and phantoms provide different scattering behaviour for structured light. This difference will guide future investigations in the simulation of light propagation through tissue-mimicking systems.

The results obtained in this paper suggest that there is a non-trivial trade-off between the advantages of employing larger OAM and VVB modes with highly separated spatial components, and the broadening of their spatial features imparted by the interaction with the media. This is also reflected on the polarization profile: indeed, while the depolarization of the OAM modes is equally affected by the media, for the VVBs, the more complex the structure (i.e., the greater the difference between m_1 and m_2), the more the polarization pattern is lost.

Disclosures

The authors declare no conflicts of interest.

References

1. V. Ntziachristos, "Going deeper than microscopy: the optical imaging frontier in biology," Nat. Methods **7**(8), 603–614 (2010).
2. D. Huang, E. Swanson, C. Lin, J. Schuman, W. Stinson, W. Chang, M. Hee, T. Flotte, K. Gregory, and C. Puliafito, "Optical coherence tomography," Science **254**(5035), 1178–1181 (1991).
3. S. Schmitz-Valckenberg, F. G. Holz, A. C. Bird, and R. F. Spaide, "Fundus autofluorescence imaging: Review and perspectives," Retina **28**(3), 385–409 (2008).

4. V. Ntziachristos, "Fluorescence molecular imaging," Annu. Rev. Biomed. Eng. **8**(1), 1–33 (2006).

5. M. R. Hee, C. R. Baumal, C. A. Puliafito, J. S. Duker, E. Reichel, J. R. Wilkins, J. G. Coker, J. S. Schuman, E. A. Swanson, and J. G. Fujimoto, "Optical coherence tomography of age-related macular degeneration and choroidal neovascularization," Ophthalmology **103**(8), 1260–1270 (1996).

6. W. Drexler, U. Morgner, R. K. Ghanta, F. X. Kärtner, J. S. Schuman, and J. G. Fujimoto, "Ultrahigh-resolution ophthalmic optical coherence tomography," Nat. Med. **7**(4), 502–507 (2001).

7. G. Guagliumi and V. Sirbu, "Optical coherence tomography: High resolution intravascular imaging to evaluate vascular healing after coronary stenting," Cathet. Cardiovasc. Intervent. **72**(2), 237–247 (2008).

8. G. W. Falk, "Autofluorescence endoscopy," Gastrointest. Endosc. Clin. **19**(2), 209–220 (2009).

9. S. Yeh, F. Forooghian, W. T. Wong, L. J. Faia, C. Cukras, J. C. Lew, K. Wroblewski, E. D. Weichel, C. B. Meyerle, H. N. Sen, E. Y. Chew, and R. B. Nussenblatt, "Fundus Autofluorescence Imaging of the White Dot Syndromes," Arch. Ophthalmol. **128**(1), 46–56 (2010).

10. C. Chi, Y. Du, J. Ye, D. Kou, J. Qiu, J. Wang, J. Tian, and X. Chen, "Intraoperative imaging-guided cancer surgery: from current fluorescence molecular imaging methods to future multi-modality imaging technology," Theranostics **4**(11), 1072–1084 (2014).

11. G. M. van Dam, G. Themelis, L. M. A. Crane, N. J. Harlaar, R. G. Pleijhuis, W. Kelder, A. Sarantopoulos, J. S. de Jong, H. J. G. Arts, A. G. J. van der Zee, J. Bart, P. S. Low, and V. Ntziachristos, "Intraoperative tumor-specific fluorescence imaging in ovarian cancer by folate receptor-a targeting: first in-human results," Nat. Med. **17**(10), 1315–1319 (2011).

12. W. F. Cheong, S. A. Prahl, and A. J. Welch, "A review of the optical properties of biological tissues," IEEE J. Quantum Electron. **26**(12), 2166–2185 (1990).

13. H. Rubinsztein-Dunlop, A. Forbes, M. V. Berry, M. R. Dennis, D. L. Andrews, M. Mansuripur, C. Denz, C. Alpmann, P. Banzer, T. Bauer, E. Karimi, L. Marrucci, M. Padgett, M. Ritsch-Marte, N. M. Litchinitser, N. P. Bigelow, C. Rosales-Guzmán, A. Belmonte, J. P. Torres, T. W. Neely, M. Baker, R. Gordon, A. B. Stilgoe, J. Romero, A. G. White, R. Fickler, A. E. Willner, G. Xie, B. McMorran, and A. M. Weiner, "Roadmap on structured light," J. Opt. **19**(1), 013001 (2017).

14. G. Milione, M. P. J. Lavery, H. Huang, Y. Ren, G. Xie, T. A. Nguyen, E. Karimi, L. Marrucci, D. A. Nolan, R. R. Alfano, and A. E. Willner, "4 × 20 gbit/s mode division multiplexing over free space using vector modes and a q-plate mode (de)multiplexer," Opt. Lett. **40**(9), 1980–1983 (2015).

15. G. Molina-Terriza, J. P. Torres, and L. Torner, "Twisted photons," Nat. Phys. **3**(5), 305–310 (2007).

16. W. B. Wang, R. Gozali, L. Shi, L. Lindwasser, and R. R. Alfano, "Deep transmission of laguerre–gaussian vortex beams through turbid scattering media," Opt. Lett. **41**(9), 2069–2072 (2016).

17. G. Molina-Terriza, L. Rebane, J. Torres, L. Torner, and S. Carrasco, "Probing canonical geometrical objects by digital spiral imaging," J. European Opt. Soc. - Rapid Publ. **2**, 07014 (2007).

18. L. Torner, J. P. Torres, and S. Carrasco, "Digital spiral imaging," Opt. Express **13**(3), 873–881 (2005).

19. L. Wang and D. Zimnyakov, Optical polarization in biomedical applications (Springer, 2006).

20. V. V. Tuchin, "Polarized light interaction with tissues," J. Biomed. Opt. **21**(7), 071114 (2016).

21. L. Allen, M. W. Beijersbergen, R. J. C. Spreeuw, and J. P. Woerdman, "Orbital angular momentum of light and the transformation of laguerre-gaussian laser modes," Phys. Rev. A **45**(11), 8185–8189 (1992).

22. M. Padgett, J. Courtial, and L. Allen, "Light's orbital angular momentum," Phys. Today **57**(5), 35–40 (2004).

23. G. Milione, H. I. Sztul, D. A. Nolan, and R. R. Alfano, "Higher-order poincaré sphere, stokes parameters, and the angular momentum of light," Phys. Rev. Lett. **107**(5), 053601 (2011).

24. L. Marrucci, E. Karimi, S. Slussarenko, B. Piccirillo, E. Santamato, E. Nagali, and F. Sciarrino, "Spin-to-orbital conversion of the angular momentum of light and its classical and quantum applications," J. Opt. **13**(6), 064001 (2011).

25. B. Cochenour, K. Morgan, K. Miller, E. Johnson, K. Dunn, and L. Mullen, "Propagation of modulated optical beams carrying orbital angular momentum in turbid water," Appl. Opt. **55**(31), C34–C38 (2016).

26. S. Mamani, L. Shi, T. Ahmed, R. Karnik, A. Rodríguez-Contreras, D. Nolan, and R. Alfano, "Transmission of classically entangled beams through mouse brain tissue," J. Biophotonics **11**(12), e201800096 (2018).

27. P. Shumyatsky, G. Milione, and R. Alfano, "Optical memory effect from polarized laguerre–gaussian light beam in light-scattering turbid media," Opt. Commun. **321**, 116–123 (2014).

28. A. Doronin, N. Vera, J. P. Staforelli, P. Coelho, and I. Meglinski, "Propagation of cylindrical vector laser beams in turbid tissue-like scattering media," Photonics **6**(2), 56 (2019).

29. K. S. Morgan, J. K. Miller, B. M. Cochenour, W. Li, Y. Li, R. J. Watkins, and E. G. Johnson, "Free space propagation of concentric vortices through underwater turbid environments," J. Opt. **18**(10), 104004 (2016).

30. I. Gianani, A. Suprano, T. Giordani, N. Spagnolo, F. Sciarrino, D. Gorpas, V. Ntziachristos, K. Pinker, N. Biton, J. Kupferman, and S. Arnon, "Transmission of vector vortex beams in dispersive media," Adv. Photonics **2**(3), 1–8 (2020).

31. L. Gong, Q. Zhao, H. Zhang, X.-Y. Hu, K. Huang, J.-M. Yang, and Y.-M. Li, "Optical orbital-angular-momentum-multiplexed data transmission under high scattering," Light: Sci. Appl. **8**(1), 27 (2019).

32. C. Gopaul and R. Andrews, "The effect of atmospheric turbulence on entangled orbital angular momentum states," New J. Phys. **9**(4), 94 (2007).

33. M. Krenn, R. Fickler, M. Fink, J. Handsteiner, M. Malik, T. Scheidl, R. Ursin, and A. Zeilinger, "Communication with spatially modulated light through turbulent air across vienna," New J. Phys. **16**(11), 113028 (2014).

34. M. Krenn, J. Handsteiner, M. Fink, R. Fickler, R. Ursin, M. Malik, and A. Zeilinger, "Twisted light transmission over 143 km," Proc. Natl. Acad. Sci. **113**(48), 13648–13653 (2016).

35. F. Bouchard, A. Sit, F. Hufnagel, A. Abbas, Y. Zhang, K. Heshami, R. Fickler, C. Marquardt, G. Leuchs, R. W. Bory, and E. Karimi, "Quantum cryptography with twisted photons through an outdoor underwater channel," Opt. Express **26**(17), 22563–22573 (2018).

36. F. Hufnagel, A. Sit, F. Grenapin, F. Bouchard, K. Heshami, D. England, Y. Zhang, B. J. Sussman, R. W. Boyd, G. Leuchs, and E. Karimi, "Characterization of an underwater channel for quantum communications in the ottawa river," Opt. Express **27**(19), 26346–26354 (2019).

37. Y. Yuan, T. Lei, S. Gao, X. Weng, L. Du, and X. Yuan, "The orbital angular momentum spreading for cylindrical vector beams in turbulent atmosphere," IEEE Photonics J. **9**(2), 1–10 (2017).

38. W. Cheng, J. W. Haus, and Q. Zhan, "Propagation of vector vortex beams through a turbulent atmosphere," Opt. Express **17**(20), 17829–17836 (2009).

39. M. Cheng, L. Guo, J. Li, J. Li, and X. Yan, "Enhanced vortex beams resistance to turbulence with polarization modulation," J. Quant. Spectrosc. Radiat. Transfer **227**, 219–225 (2019).

40. D. Cozzolino, E. Polino, M. Valeri, G. Carvacho, D. Bacco, N. Spagnolo, L. K. Oxenløwe, and F. Sciarrino, "Air-core fiber distribution of hybrid vector vortex-polarization entangled states," Adv. Photonics **1**(4), 1 (2019).

41. A. Sit, F. Bouchard, R. Fickler, J. Gagnon-Bischoff, H. Larocque, K. Heshami, D. Elser, C. Peuntinger, K. Günthner, B. Heim, C. Marquardt, G. Leuchs, R. W. Boyd, and E. Karimi, "High-dimensional intracity quantum cryptography with structured photons," Optica **4**(9), 1006–1010 (2017).

42. G. Vallone, V. D'Ambrosio, A. Sponselli, S. Slussarenko, L. Marrucci, F. Sciarrino, and P. Villoresi, "Free-space quantum key distribution by rotation-invariant twisted photons," Phys. Rev. Lett. **113**(6), 060503 (2014).

43. D. Cozzolino, D. Bacco, B. Da Lio, K. Ingerslev, Y. Ding, K. Dalgaard, P. Kristensen, M. Galili, K. Rottwitt, S. Ramachandran, and L. K. Oxenløwe, "Orbital angular momentum states enabling fiber-based high-dimensional quantum communication," Phys. Rev. Appl. **11**(6), 064058 (2019).

44. J. Kupferman and S. Arnon, "Zero-error attacks on a quantum key distribution fso system," OSA Continuum **1**(3), 1079–1086 (2018).

45. B. Ndagano, I. Nape, M. A. Cox, C. Rosales-Guzman, and A. Forbes, "Creation and detection of vector vortex modes for classical and quantum communication," J. Lightwave Technol. **36**(2), 292–301 (2018).

46. Y. Baykal, M. C. Gökçe, and Y. Ata, "Anisotropy effect on performance of subcarrier intensity modulated binary phase shift keying optical wireless communication links in weakly turbulent underwater channel," J. Mod. Opt. **66**(19), 1871–1875 (2019).

47. J. H. Shapiro, "Near-field turbulence effects on quantum-key distribution," Phys. Rev. A **67**(2), 022309 (2003).

48. J. Kupferman and S. Arnon, "Decoding algorithm for vortex communications receiver," J. Opt. **20**(1), 015702 (2018).

49. J. Kupferman and S. Arnon, "Direct detection receiver for vortex beam," J. Opt. Soc. Am. A **35**(9), 1543–1548 (2018).

50. A. E. Willner, H. Huang, Y. Yan, Y. Ren, N. Ahmed, G. Xie, C. Bao, L. Li, Y. Cao, Z. Zhao, J. Wang, M. P. J. Lavery, M. Tur, S. Ramachandran, A. F. Molisch, N. Ashrafi, and S. Ashrafi, "Optical communications using orbital angular momentum beams," Adv. Opt. Photonics **7**(1), 66–106 (2015).

51. I. B. Djordjevic, "Multidimensional qkd based on combined orbital and spin angular momenta of photon," IEEE Photonics J. **5**(6), 7600112 (2013).

52. F. Graffitti, V. D'Ambrosio, M. Proietti, J. Ho, B. Piccirillo, C. de Lisio, L. Marrucci, and A. Fedrizzi, "Hyperentanglement in structured quantum light," arXiv preprint arXiv:2006.01845 (2020).

53. M. Anastasopoulou, M. Koch, D. Gorpas, A. Karlas, U. Klemm, P. B. Garcia-Allende, and V. Ntziachristos, "Comprehensive phantom for interventional fluorescence molecular imaging," J. Biomed. Opt. **21**(9), 091309 (2016).

54. D. Gorpas, M. Koch, M. Anastasopoulou, U. Klemm, and V. Ntziachristos, "Benchmarking of fluorescence cameras through the use of a composite phantom," J. Biomed. Opt. **22**(1), 016009 (2017).

55. B. Zhu, I.-C. Tan, J. Rasmussen, and E. Sevick-Muraca, "Validating the sensitivity and performance of near-infrared fluorescence imaging and tomography devices using a novel solid phantom and measurement approach," Technol. Cancer Res. Treat. **11**(1), 95–104 (2012).

56. P. Krauter, S. Nothelfer, N. Bodenschatz, E. Simon, S. Stocker, F. Foschum, and A. Kienle, "Optical phantoms with adjustable subdiffusive scattering parameters," J. Biomed. Opt. **20**(10), 105008 (2015).

57. F. Cardano, E. Karimi, S. Slussarenko, L. Marrucci, C. de Lisio, and E. Santamato, "Polarization pattern of vector vortex beams generated by q-plates with different topological charges," Appl. Opt. **51**(10), C1–C6 (2012).

58. T. Giordani, E. Polino, S. Emiliani, A. Suprano, L. Innocenti, H. Majury, L. Marrucci, M. Paternostro, A. Ferraro, N. Spagnolo, and F. Sciarrino, "Experimental engineering of arbitrary qudit states with discrete-time quantum walks," Phys. Rev. Lett. **122**(2), 020503 (2019).

59. F. Cardano, M. Maffei, F. Massa, B. Piccirillo, C. de Lisio, G. De Filippis, V. Cataudella, E. Santamato, and L. Marrucci, "Statistical moments of quantum-walk dynamics reveal topological quantum transitions," Nat. Commun. **7**(1), 11439 (2016).

60. L. Marrucci, C. Manzo, and D. Paparo, "Optical spin-to-orbital angular momentum conversion in inhomogeneous anisotropic media," Phys. Rev. Lett. **96**(16), 163905 (2006).